SANDIA REPORT
SAND2011-9005
Unlimited Release
Printed December 2011

Final LDRD report: Science-based Solutions to Achieve High-performance Deep-UV Laser Diodes

Mary H. Crawford, Andrew A. Allerman, Andrew M. Armstrong, Mary A. Miller, Michael L. Smith, Karl R. Westlake, Karen C. Cross, Stephen R. Lee, Tanya A. Henry and Leonard J. Alessi

Prepared by
Sandia National Laboratories
Albuquerque, New Mexico 87185 and Livermore, California 94550

Sandia National Laboratories is a multi-program laboratory managed and operated by Sandia Corporation, a wholly owned subsidiary of Lockheed Martin Corporation, for the U.S. Department of Energy's National Nuclear Security Administration under contract DE-AC04-94AL85000.

Issued by Sandia National Laboratories, operated for the United States Department of Energy by Sandia Corporation.

Available to DOE and DOE contractors from
U.S. Department of Energy
Office of Scientific and Technical Information
P.O. Box 62
Oak Ridge, TN 37831

Telephone: (865) 576-8401
Facsimile: (865) 576-5728
E-Mail: reports@adonis.osti.gov
Online ordering: http://www.osti.gov/bridge

Available to the public from
U.S. Department of Commerce
National Technical Information Service
5285 Port Royal Rd.
Springfield, VA 22161

Telephone: (800) 553-6847
Facsimile: (703) 605-6900
E-Mail: orders@ntis.fedworld.gov
Online order: http://www.ntis.gov/help/ordermethods.asp?loc=7-4-0#online

SAND2011-9005
Unlimited Release
Printed December 2011

Final LDRD report: Science-based Solutions to Achieve High-performance Deep-UV Laser Diodes

Mary H. Crawford, Andrew M. Armstrong, Michael L. Smith,
Karl R. Westlake, Stephen R. Lee and Tanya A. Henry
Semiconductor Material and Device Sciences Department

Andrew A. Allerman, Karen C. Cross, and Leonard J. Alessi
Advanced Materials Sciences Department

Mary A. Miller
Validation and Failure Analysis Department

Sandia National Laboratories
P.O. Box 5800
Albuquerque, New Mexico 87185-MS1086

Abstract

We present the results of a three year LDRD project that has focused on overcoming major materials roadblocks to achieving AlGaN-based deep-UV laser diodes. We describe our growth approach to achieving AlGaN templates with greater than ten times reduction of threading dislocations which resulted in greater than seven times enhancement of AlGaN quantum well photoluminescence and 15 times increase in electroluminescence from LED test structures. We describe the application of deep-level optical spectroscopy to AlGaN epilayers to quantify deep level energies and densities and further correlate defect properties with AlGaN luminescence efficiency. We further review our development of p-type short period superlattice structures as an approach to mitigate the high acceptor activation energies in AlGaN alloys. Finally, we describe our laser diode fabrication process, highlighting the development of highly vertical and smooth etched laser facets, as well as characterization of resulting laser heterostructures.

ACKNOWLEDGMENTS

The authors gratefully acknowledge Blythe Clark, and Qiming Li for providing assistance in materials characterization. We appreciate the support of managers Dan Barton (project manager), Robert Biefeld, and Jerry Simmons throughout this work.

CONTENTS

FIGURES

TABLES

NOMENCLATURE

AFM	Atomic force microscopy
CL	Cathodoluminescence
CW	Continuous wave
DLOS	Deep level optical spectroscopy
EL	Electroluminescence
FIB	Focused ion beam
FWHM	Full width at half maximum
GS-MBE	Gas source molecular beam epitaxy
ICP	Inductively coupled plasma
IQE	Internal quantum efficiency
LD	Laser diode
LDRD	Laboratory directed research and development
LED	Light-emitting diode
MOVPE	Metal-organic vapor phase epitaxy
MQW	Multi-quantum well
NIC	Nomarski interference contrast
NRC	Non-radiative recombination center
PL	Photoluminescence
QW	Quantum well
TMAl	Trimethyl aluminum
TMGa	Trimethyl gallium
SEM	Scanning electron microscopy
SPSL	Short period superlattice
SIMS	Secondary ion masss
SSPC	Steady-state photocapacitance
T_g	Growth temperature
τ_{nr}	nonradiative lifetme
UID	Unintentionally doped
UV	Ultraviolet
XRD	X-ray diffraction

1. INTRODUCTION

While a number of mission-critical applications would benefit from a compact, deep ultraviolet laser diode (LD) at custom wavelengths, commercial laser diodes (LDs) are currently limited to wavelengths of 365 nm and longer. AlGaN alloys are the most promising materials for deep UV LDs, with the recent demonstration of mW-level 250-340 nm AlGaN light-emitting diodes.[1] To date, the shortest wavelength reported for AlGaN LDs is 336 nm.[2] Moving to shorter wavelengths has been thwarted by a lack of fundamental insight and solutions to key AlGaN materials challenges. In this report, we present results from a three year LDRD project to first, address these materials challenges, and second, integrate solutions into AlGaN UV LD structures. Section 2 describes the key AlGaN materials challenges that we addressed in this project. Section 3 provides details of our materials research and accomplishments. Section 4 describes our laser development including ridge waveguide laser processing and laser diode testing. Finally, conclusions are summarized in Section 5.

2. CHALLENGES OF ALGAN-BASED UV EMITTERS

A major factor in the lack of progress in AlGaN LDs is the fact that materials challenges are present throughout the LD heterostructure (Figure 1). Starting at the top of the structure, we note that p-type doping is intrinsically difficult because these dopants (acceptors) have energy levels > 200 meV from the valence band, resulting in extremely low activation of free holes at room temperature (kT~26 meV). As acceptor activation energy increases with bandgap, p-type doping is increasingly difficult for shorter UV-wavelength materials. The light-emitting region is comprised of a series of ~ 2 nm-thick AlGaN quantum wells (QWs) surrounded by higher bandgap AlGaN barriers. These layers can have relatively low optical efficiency that is likely due to crystalline defects, although the nature of these defects is not well known. Due to a lack of commercial AlGaN substrates, the p-type cladding, QWs and n-type cladding device layers are typically grown on dissimilar substrate materials such as sapphire. The large discrepancy in atomic spacing (lattice constant) between AlGaN and sapphire results in high densities (>5e9 cm^{-2}) of extended defects (threading dislocations). These defects can limit optical efficiency and device reliability and are some 4 orders of magnitude higher than other III-V semiconductors grown on native substrates. We note that commercial AlN substrates with TD densities of <1e6 cm^{-2} are becoming available but are not lattice-mismatched with several-micron-thick AlGaN LD epilayers. Generally, all substrates under consideration have polar orientations (e.g., [0001] wurzite), leading to polarization discontinuities between the layers in the structure, strong internal electric fields (~MV/cm), and band-bending. While often detrimental, we show below how these fields may alleviate p-type doping challenges. Below we describe our efforts to first understand and overcome these materials challenges, and second, apply new materials developments to 300-340 nm laser structures.

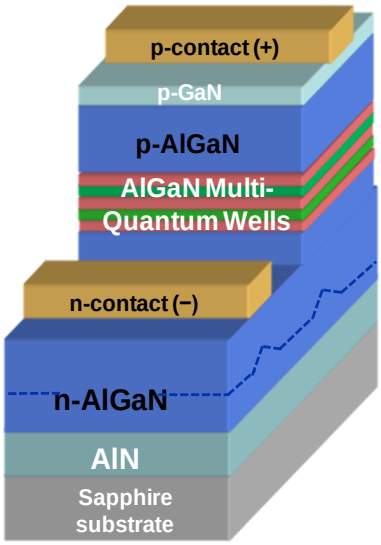

Figure 1: AlGaN laser diode heterostructure (not to scale)

3. MATERIALS SOLUTIONS

3.1 Development of low-dislocation AlGaN templates

We developed a method to produce $Al_xGa_{1-x}N$ (x ~ 0.30) epilayers with dislocation densities of low 10^8 cm^{-2} that are suitable for UV laser diodes and LEDs. The method has the benefits of eliminating defects threading from mesa regions but without the uses of faceted GaN pyramids.[2,3] It avoids the use of GaN epilayers that would absorb emission of bottom emitting UV LEDs. The method results in an epilayer with uniform dislocation density across a wafer and consequently, is well suited for large area devices such as LEDs and eliminates the need for precise alignment of the ridge of a laser diode to the underlying growth. These advantages are obtained while doping with Si, enabling lower n-type sheet resistances that lower operating voltage or simplify the fabrication of vertically conducting devices. Furthermore, the method is demonstrated using 2 inch wafers, using growth conditions typical for AlGaN without the need for higher temperatures. The surface is smooth and free of pits, suitable for subsequent growth of device layers and processing without prior CMP polishing.

All group-III nitride layers were grown by metal-organic vapor phase epitaxy (MOVPE) in a Veeco D-125 reactor at 75 torr. Conventional precursors, including trimethylgallium (TMGa), trimethylaluminum (TMAl), and ammonia, were used to grow $Al_xGa_{1-x}N$ alloys, and silane was used as a dopant. Nitrogen and hydrogen were used as carrier gases. AlGaN templates used in this work consisted of 3 μm thick, Si doped $Al_{0.32}Ga_{0.68}N$ ($N_o = 3x10^{18}$ cm^{-2}) grown on top of 1.9 μm thick, AlN grown on (0001) c-plane sapphire substrates mis-oriented 0.2° toward the m-plane. The $Al_{0.32}Ga_{0.68}N$ layer was grown at 1050 °C, the same pyrometer temperature used for the growth of GaN, using a group-III molar flux of 60 μmoles/min and an Al/group-III ratio of 0.34. The dislocation density of the AlN ($Al_{0.32}Ga_{0.68}N$) templates varied from 3-6 x 10^9 (2-3 x 10^9) cm^{-2} as determined from x-ray diffraction measurements.[4]

Once the initial group-III nitride template (AlN or $Al_{0.32}Ga_{0.68}N$) was grown, conventional photolithography was used to pattern parallel stripes consisting of micron wide mesas separated by micron wide trenches formed by inductively coupled plasma (ICP) etching. (Figure 2a, b) The trenches were aligned in the $<1\text{-}100>_{AlN}$ and thus perpendicular to the major flat of the sapphire substrate. After removal of the etch mask, 4 to 12 μm of $Al_{0.32}Ga_{0.68}N$ was grown over the patterned nitride template with the growth conditions used for the $Al_{0.32}Ga_{0.68}N$ template.

The surface morphology was evaluated using Nomarski interference contrast (NIC) microscopy and atomic force microscopy (AFM). Sheet resistance measurements were made using a Lehighton contactless resistivity system. Following characterization of the overgrown $Al_{0.32}Ga_{0.68}N$ layer, a GaN/AlGaN multi-quantum well structure regrown for cathodoluminescence (CL). Dislocations are revealed as "dark spots" in the CL image enabling the determination of areal density and spatial distribution. Monochromatic images were taken using a MonoCL system by Gatan on a FEI NanoSEM 200. An accelerating voltage of 3kV and a beam current of ~3.6 nA were selected to minimize excitation volume while still providing sufficient signal and contrast to clearly resolve dislocations.

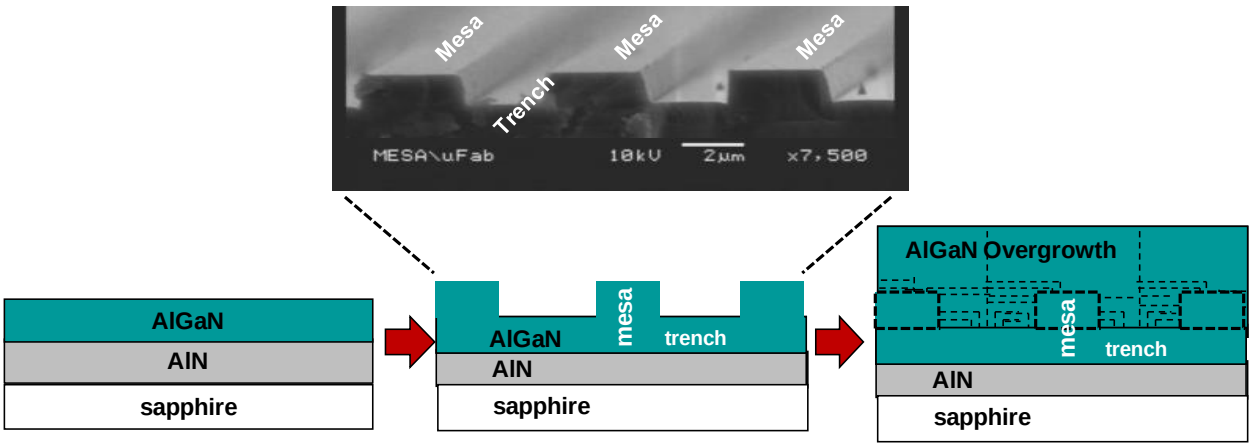

Figure 2: Process flow of patterning and AlGaN overgrowth developed to produce AlGaN templates with a dislocation density of 2-3x10^8 cm^{-2}

Room temperature photoluminescence (PL) was used to assess the improvement in the optical efficiency of GaN-AlGaN multi-quantum well (MQW) structure. Measurements were carried out using a Nanometrics RPM2000 photoluminescence mapper employing a 266 nm pump laser. AlGaN composition was confirm by X-ray diffraction measurements made using a Philips X'Pert Pro diffractometer equipped with a hybrid monochromator delivering Cu $K\alpha_1$ x-rays and an asymmetric (220) Ge diffracted-beam analyzer. Dislocation density of planar templates was estimated from the FWHM of rocking curves made of the (00.4) and (10.1) reflections using the method described by Lee.[4]

The spatial distribution and density of threading dislocations are shown in the monochromatic cathodoluminenescence image (Figure 3a) of a typical starting AlGaN template prior to patterning. The dislocation density cannot be accurately determined from CL due to the high dislocation density in the AlGaN epilayer but a dislocation density of ~ 4 x 10^9 cm^{-2} was determined by x-ray diffraction measurements. Following pattering, trench formation by etching and overgrowth of 7 µm of AlGaN, CL shows that the dislocation is reduced to 2-3 x $10^8 cm^{-2}$ (Figure 3b). The annihilation of dislocations induced by AlGaN overgrowth of the etched trenches is responsible for the greater than 10 x reduction in dislocation density from the starting AlGaN template. The CL image in Figure 3c shows that the dislocation density is spatially uniform over large, device size areas and consequently is well suited for large area devices such as LEDs and eliminates the need for precise alignment of the ridge of a laser diode to the underlying growth. These advantages are obtained while doping with Si, enabling lower n-type sheet resistances that lower operating voltage or simplify the fabrication of vertically conducting devices. Furthermore, the method uses growth conditions typical for AlGaN without the need for higher temperatures.

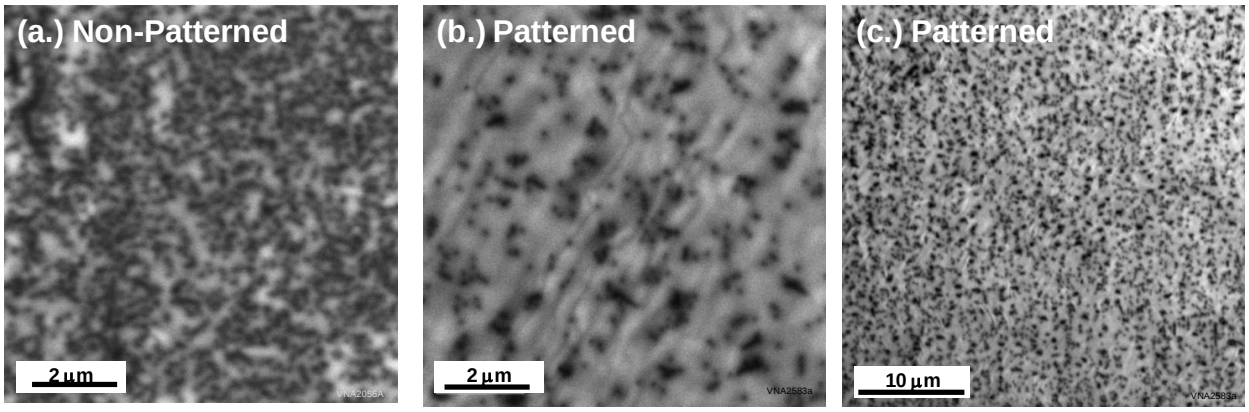

Figure 3: Cathodoluminescence of (a) starting template and (b,c) after 7 mm of AlGaN overgrowth showing a greater than 10x reduction in dislocation density (to 2-3x10^8 cm^{-2}) using patterned overgrowth process.

AFM images (Figure 4a and 4b) of 6 μm of AlGaN overgrowth show that the surface is free of pits or modulation from the underling pattern consisting of 1 μm wide trenches separated by 1 μm wide mesas. The RMS roughness is 1.2 nm over a 10 x 10 μm^2 region and 0.37 nm over a 3 x 3 μm^2 region. Figure 5 shows a Normaski DIC photograph taken at 50x of the same sample in Figure 4. The surface of overgrown AlGaN layer is suitable for the growth of device layers.

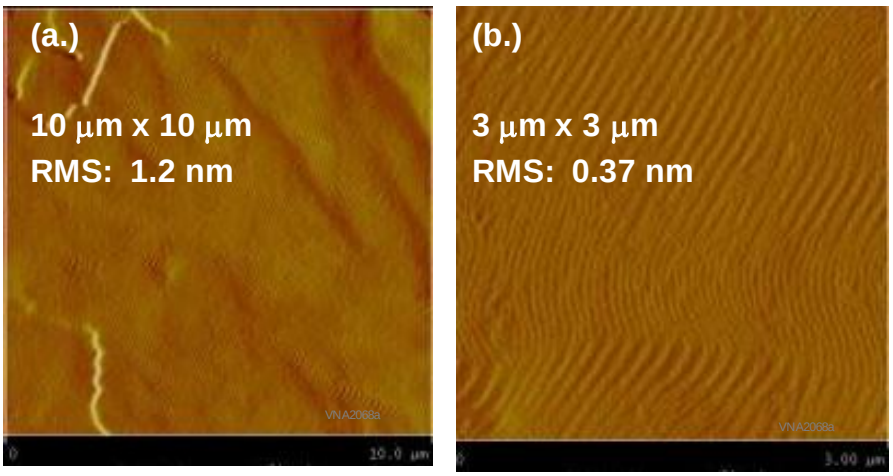

Figure 4: AFM images of 6 μm of AlGaN overgrowth. (a) 10 x 10 μm^2 sized image (b) 3 x 3 μm^2 sized image.

Figure 5: Nomarski DIC image, taken at 50x, of 6 μm of AlGaN overgrowth

Room temperature photoluminescence (PL) emission from GaN-AlGaN multi-quantum wells (MQWs) consistently showed a 7 to 8 x increase when grown on AlGaN overgrown patterned templates compared to growth on non-patterned AlGaN templates. Figure 6 shows the PL emission spectra for QWs grown on a AlGaN grown over a template patterned with 6 μm wide trenches separated by 1 μm wide mesas. The increased QW emission is indicative of higher quality material with a lower density of non-radiative defects and is consistent with CL measurements showing lower dislocation density for AlGaN epilayers grown over patterned templates.

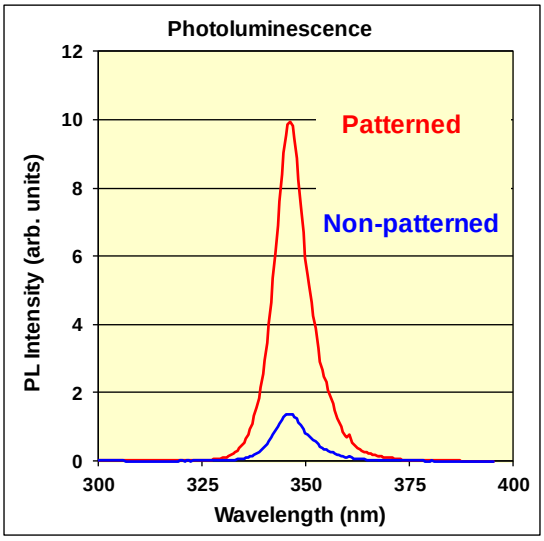

Figure 6: Room temperature PL from GaN-AlGaN multi-quantum wells grown on patterned (red) and non-patterned (blue) AlGaN templates.

The improvement in material quality associated with reduced dislocation density was also observed in continuous wave (CW) electroluminescence (EL) spectra from test LEDs fabricated from laser diode structures. Figure 7 shows the EL from laser diode structures grown on either 10 μm of AlGaN grown over a 6 μm wide trenches separated by 1 μm mesas or 5 μm of AlGaN

grown over 1 μm wide trenches separated by 1 μm wide trenches. In both cases, the EL is approximately 15 x higher than that grown on a non-patterned AlGaN template. We see that a roughly 20x reduction in dislocation density results in greater than an order of magnitude increase in electroluminescence. Observing that PL emission increased by ~ 7x from MQWs and EL emission by ~ 15x when patterned templates are used, it is likely that not only is the radiative efficiency of the MQWs increased, but carrier transport is also measurably improved by reducing the dislocation density of the epilayers.

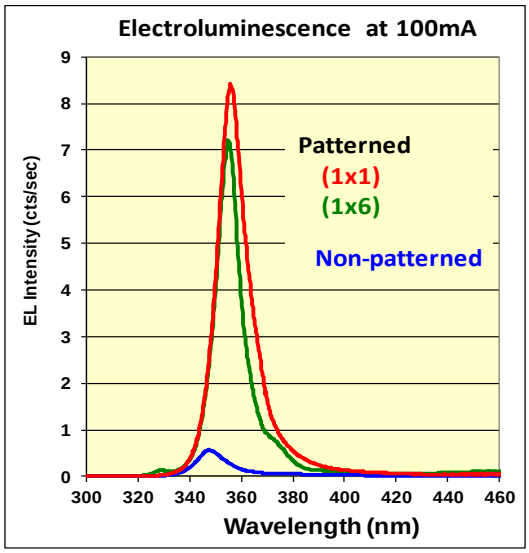

Figure 7: Electroluminescence from test LEDs made from laser diode heterostructures grown on patterned (red, green) and non-patterned (blue) AlGaN templates.

Some further reduction in dislocation density is possible by repeating the patterning and overgrowth sequence a second time. Figure 8 shows the CL image from a sample that initially was patterned and overgrown with 4 μm of undoped AlGaN. The wafer was then patterned a 2nd time and overgrown with 10 μm of AlGaN. No effort was made to align the second patterning with the first. The final layer was crack free with a nicely coalesced surface, free of pits. The dislocation density from CL was 1.7 x10^{8} cm^{-2}, somewhat lower than that achieved with the single patterning and overgrowth sample in Figure 7. Again, threading dislocations are randomly distributed over the surface of the wafer, eliminating the need for aligning laser diodes to the underlying pattern and providing device-size areas for LEDs.

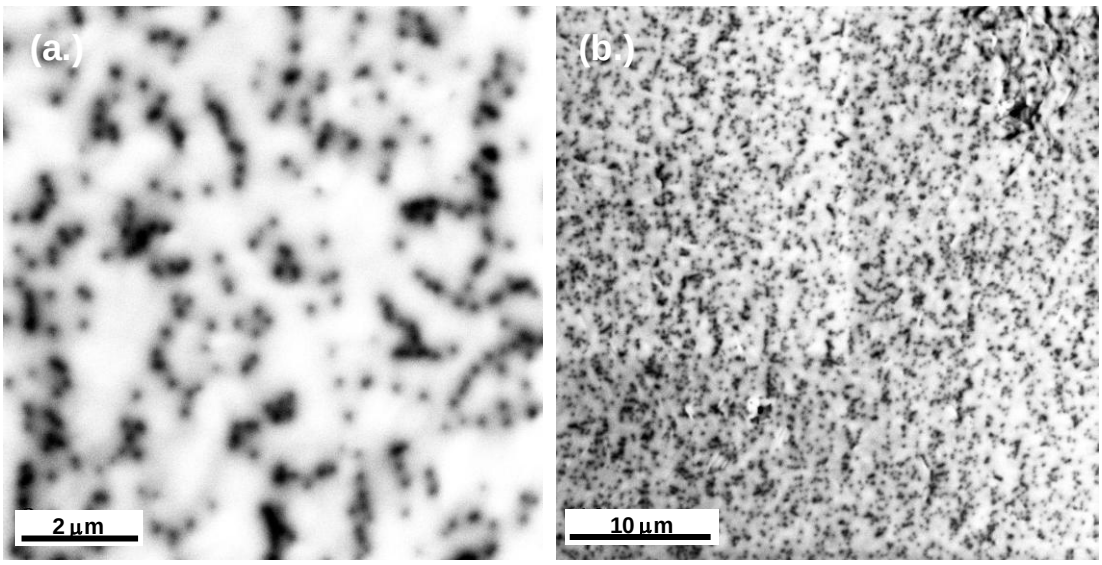

Figure 8: Cathodoluminescence of GaN-AlGaN MQWs grown on an AlGaN template achieved by two pattern and overgrowth sequences.

In summary, we have developed a method of reducing the density of threading dislocations in AlGaN epilayers to low 10^8 cm^{-2} over 2" wafer-size areas. Further, we observe a 7 x in PL emission and 15 x in EL emission from MQWs and laser diode structures grown on low dislocation density templates produced by AlGaN overgrowth patterned templates.

3.2 Study of the impact of point defects in AlGaN

A critical aspect to optimizing the performance of an LED or LD is maximizing the internal quantum efficiency (IQE) of the multi-quantum well (MQW) region. An important issue to improving IQE is understanding and mitigating the role of defects in the MQW region that act as non-radiative recombination centers (NRCs) and reduce the non-radiative lifetime (τ_{nr}).[5] The deleterious influence of extended defects on AlGaN radiative efficiency has been studied previously for a variety of substrates.[6,7,8] However, there are few studies correlating the influence of AlGaN MQW growth conditions, point defect incorporation, and optical efficiency. Recent time-resolved cathodoluminescence and positron annihilation spectroscopy experiments determined that point defects rather than extended defects can dominate the radiative properties of AlN.[9] In this work, photoluminescence (PL) and deep level optical spectroscopy (DLOS) were used in concert to quantify the influence of growth temperature (T_g) on point defect incorporation and to study the resultant impact on UV photoluminescence of AlGaN/(Al)GaN MQWs.

Unintentionally-doped (UID) $Al_{0.2}Ga_{0.8}N/Al_xGa_{1-x}N$ MQWs (x = 0, 0.05) targeting 340 nm emission were grown by MOVPE using standard precursors and H_2 carrier gas. A template comprised of a 1.9 µm AlN layer followed by a 3.6 µm $Al_{0.3}Ga_{0.7}N$ layer was grown upon a sapphire substrate, producing ~ 5×10^9 cm^{-2} threading dislocation density as determined by x-ray diffraction measurements of symmetric (00.2) and asymmetric (10.1) reflections. One set of MQWs consisted of a 75 Å $Al_{0.2}Ga_{0.8}N$ spacer, six periods of 25 Å/75 Å $GaN/Al_{0.2}Ga_{0.8}N$

MQWs, and a 300 Å $Al_{0.3}Ga_{0.7}N$ capping layer, where T_g was varied from 1010 ºC to 1060 ºC. A second series of $Al_{0.2}Ga_{0.8}N/Al_{0.05}Ga_{0.95}N$ MQWs were also grown to compare PL trends as a function of T_g for both GaN and AlGaN wells. $Al_{0.2}Ga_{0.8}N/Al_{0.05}Ga_{0.95}N$ MQWs were grown on nominally identical templates with nominally identical structure, except the $Al_{0.05}Ga_{0.95}N$ well region had a thickness of 35 Å, and T_g therein was varied between 1060 ºC and 1080 ºC.

Figure 9 shows the integrated PL intensity of the $Al_{0.2}Ga_{0.8}N/GaN$ and $Al_{0.2}Ga_{0.8}N/Al_{0.05}Ga_{0.95}N$ MQWs as a function of T_g using 266 nm laser excitation at an intensity of 43 mW/cm^2. For the MQWs with GaN wells, > 5x increase in PL intensity was observed when T_g was increased from 1010 ºC to 1060 ºC. A similar trend of enhanced PL with increasing T_g was also observed for $Al_{0.2}Ga_{0.8}N/Al_{0.05}Ga_{0.95}N$ MQWs. The increase in PL cannot be attributed to polarization-related effects such as the QCSE, as MQWs within their respective sample set had a nominally identical aluminum content, well width and strain state. Moreover, similar light extraction efficiency from the MQWs was expected since no notable change in surface morphology or roughness with T_g was observed by AFM. The MQW samples were grown on similar substrates and template layers, discounting any influence of threading dislocations on the observed variation in PL intensity. Hence, improved PL output with increasing T_g was attributed to reduced point defect incorporation in the MQW region.

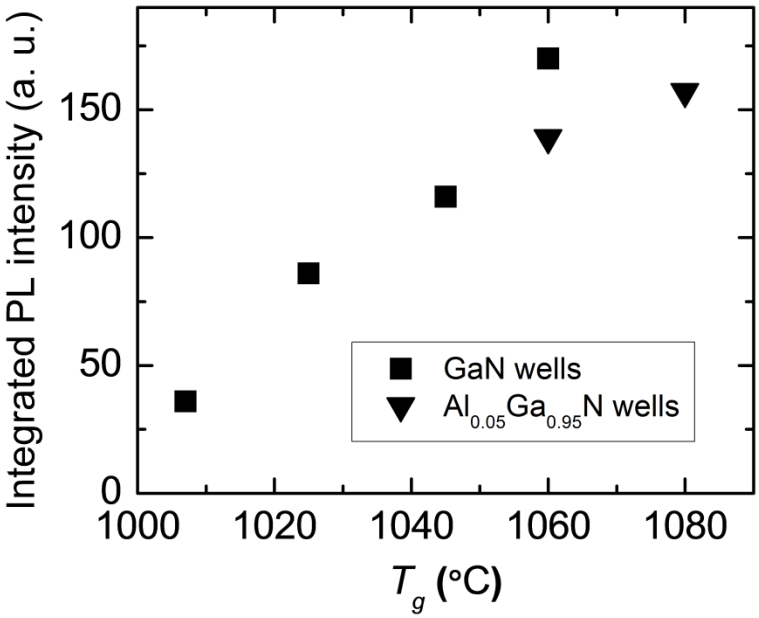

Figure 9: Integrated MQW PL intensity as a function of well region T_g.

To further investigate this hypothesis, DLOS and steady-state photocapacitance (SSPC) were employed to quantitatively correlate the relationship between T_g and point defect incorporation under MQW growth conditions. DLOS is a differential photocapacitance technique that determines the spectral variation of a deep level defect optical cross-section (σ^o) as a function of photon energy ($h\nu$). Fitting σ^o to an appropriate theoretical model[8,9] determines the optical photoionization energy (E^o) and, in the case of significant lattice relaxation, the Franck-Condon energy (d_{FC}) of the defect state. Detailed analysis of DLOS has been given previously.[10] The deep level defect density (N_t) was determined from SSPC using the typical expression N_t =

$2N_d\Delta C/C_0$, where N_d is the apparent space-charge density as measured from capacitance-voltage analysis, C_0 is the equilibrium diode capacitance and ΔC is photocapacitance upon deep level photoemission. DLOS and SSPC measurements were performed on Schottky diodes (as described below) at room temperature using a broadband Xe lamp coupled to a ¼ meter monochromator and mode-sorting filters to scan $1.20 < h\nu < 3.80$ eV with 0.025 eV resolution.

Direct application of DLOS to the MQW samples was not possible because DLOS and SPSC are electrically sensitive, while the MQW samples lacked electrical contact layers. To overcome this challenge, tailored UID-$Al_{0.08}Ga_{0.92}N$/*n*-GaN:Si Schottky diode heterostructures were designed to preserve the growth conditions of MQW well regions while enabling DLOS and SSPC. The UID-$Al_{0.08}Ga_{0.92}N$ cap layer of a Schottky diode emulates the well region of MQWs, while the *n*-GaN region (which is not relevant to MQWs) provides electrical access. Slightly higher aluminum content was included in the DLOS heterostructures to provide better depth resolution, as discussed shortly. The utility of the UID-$Al_{0.08}Ga_{0.92}N$/*n*-GaN:Si design for deep level defect spectroscopy becomes evident by considering that DLOS and SSPC are only sensitive to deep level defects residing in depleted regions of a diode. For the present case of metal-face growth, polarization effects will deplete the UID-$Al_{0.08}Ga_{0.92}N$ cap of the Schottky diode and form a two-dimensional electron gas at the $Al_{0.08}Ga_{0.92}N$/GaN heterointerface, producing an abrupt demarcation between the depleted $Al_{0.08}Ga_{0.92}N$ cap and accumulated *n*-GaN layer. The greater aluminum contrast of the Schottky diode heterostructures compared to the MQWs sharpens this delineation. Thus, DLOS measurements of the UID-$Al_{0.08}Ga_{0.92}N$/*n*-GaN diodes should be exclusively sensitive to the deep levels of interest located in the UID-$Al_{0.08}Ga_{0.92}N$ cap that emulates the well region of a MQW and have no sensitivity to deep levels related to the underlying *n*-GaN region.

UID-$Al_{0.08}Ga_{0.92}N$/*n*-GaN:Si Schottky diodes were grown and processed for DLOS and SSPC measurements. Diodes were grown on *n*-GaN:Si templates on sapphire with threading dislocation density ~ 5×10^8 cm^{-2}. For each DLOS sample, a 1000 nm thick Si-doped (~ 3×10^{18} cm^{-3}) GaN layer was grown at 1025 ºC, followed by growth of a UID-AlGaN cap layer of 300 nm thickness at either T_g = 1010 ºC or 1060 ºC. Apart from the small variation in aluminum content, the UID-$Al_{0.08}Ga_{0.92}N$ cap layers were grown under conditions nominally identical to the well region of the $Al_{0.2}Ga_{0.8}N/Al_{0.05}Ga_{0.95}N$ MQW samples, so the T_g-dependence of the type and density of defects observed via DLOS for the former were expected to be representative of defects incorporating in the latter. A control DLOS sample was also grown with a 1000 nm thick lightly Si-doped (~ 3×10^{16} cm^{-3}) GaN layer rather than an AlGaN cap. DLOS samples were patterned into Schottky diodes using ICP etching to form AlGaN mesas and expose the underlying *n*-GaN region. Electron beam evaporation was used to deposit semi-transparent nickel contacts of 9 nm thickness on the AlGaN surface and Ti/Al/Ni/Au stacks on the *n*-GaN to form lateral ohmic contacts.

DLOS measurements of the UID-AlGaN/*n*-GaN and *n*-GaN control diodes taken at 0 V bias are shown in Figure 10. The symbols are data and the lines are fits to the models of Lucovksy[11] or Pässler.[12] The data were offset for clarity since relative spectral variations of the DLOS spectra are sufficient to characterize the defect states. Note that DLOS measures deep level energy but does not quantify N_t; N_t measurement is discussed later. DLOS of the *n*-GaN control sample unambiguously identified GaN-related defects. The absence of *n*-GaN-related defect states in

the DLOS spectra of the UID-AlGaN/*n*-GaN samples confirms the desired selectivity to the UID-AlGaN cap layer. Selective DLOS sensitivity to AlGaN-related defects over GaN in the UID-AlGaN/*n*-GaN samples is further evidenced by the ~3.6 eV AlGaN band edge peaks in lieu of a GaN band edge peak at ~ 3.4 eV.

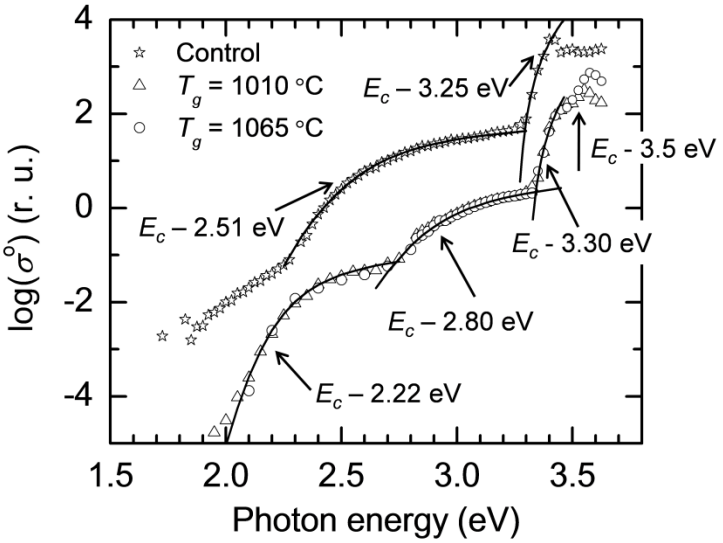

Figure 10: DLOS spectra of the *n*-GaN control sample and the UID-AlGaN/*n*-GaN heterostructures with different T_g for the UID-AlGaN cap layers. The symbols are data and the lines are theoretical fits. The E_c – 2.22 eV and E_c – 2.80 eV spectra were fit to the model in Ref. 13, and the E_c – 3.30 eV level was fit to the model in Ref. 11.

Since the deep levels observed for the *n*-GaN control sample are not relevant to MQWs, the focus now turns to the AlGaN-related deep levels and their dependence on T_g. The similarity of the AlGaN DLOS spectra of Figure 10 shows that the type of deep level defects incorporating under MQW growth conditions did not change as T_g was increased by 55 ºC. The E_c – 2.22 eV (d_{FC} = 0.10 eV) and E_c – 2.80 eV (d_{FC} = 0.23 eV) defect levels showed broad DLOS thresholds, indicating significant lattice relaxation. Conversely, the E_c – 3.30 eV and E_c – 3.5 eV levels exhibited sharp onsets, indicating effective mass-like defect states. The 3.5 eV onset was too close to the band edge to resolve precisely, so E^o of the corresponding defect level was estimated to be coincident with its threshold energy. The energetic position of the E_c – 2.80 eV level in the AlGaN band gap is similar to that reported for the group-III vacancy (V_{III}) complexed with an impurity,[13] while the E_c – 3.30 eV defect state is probably related to the E_c – 3.22 eV level that is commonly reported for MOVPE-grown *n*-GaN but whose origin remains speculative.[14,15] The microscopic origin of the AlGaN defect levels at E_c – 2.22 eV and E_c – 3.5 eV will be the subject of future investigation.

While increasing T_g by 50 ºC did not affect the types of deep level defects incorporating under MQW growth conditions, the deep level densities were markedly reduced. Figure 11 shows the SSPC spectra of the AlGaN cap layers, and N_t data are recapitulated in the inset table, where a net N_t is reported for the closely-spaced E_c – 3.30 eV and E_c – 3.50 eV levels. Substantial reduction in N_t along with strong increase in MQW PL intensity, both observed with increased T_g, suggests strongly that non-radiative defect centers located in the well region are deleterious to PL efficiency. Reduction of N_t then improved MQW PL intensity by increasing τ_{nr} and hence

IQE. It is possible that reduction of N_t in the MQW barriers with increased T_g could have also contributed to improved PL intensity since the barriers were also optically pumped. Barrier defect states can influence PL efficiency by impeding transport of carriers optically excited in the barriers to the quantum wells and also by forming non-radiative recombination channels accessible to carriers localized in the quantum wells due to finite wave function penetration into the barriers.

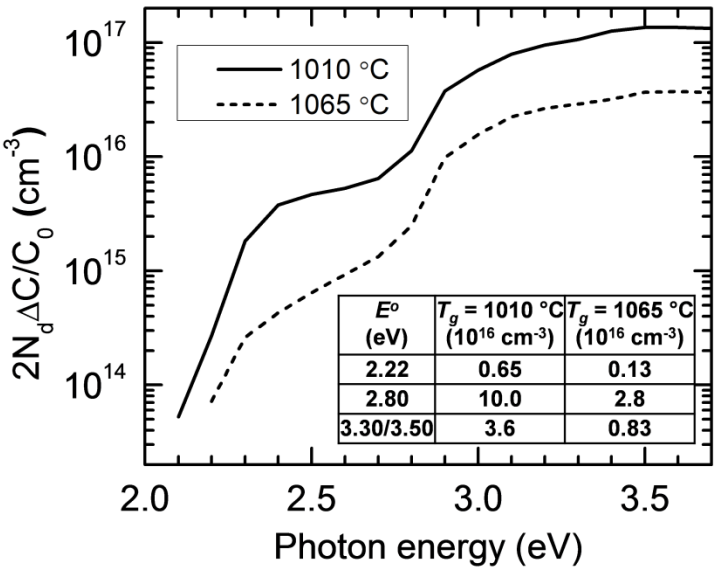

E^o (eV)	T_g = 1010 °C (10^{16} cm^{-3})	T_g = 1065 °C (10^{16} cm^{-3})
2.22	0.65	0.13
2.80	10.0	2.8
3.30/3.50	3.6	0.83

Figure 11: SSPC spectra of the UID-AlGaN/*n*-GaN heterostructures with different T_g for the UID-AlGaN cap layers. N_t data are summarized in the inset table.

It is not clear which well-region deep level most impacts τ_{nr}. The combined density of the E_c – 3.30 eV/E_c – 3.50 eV tandem decreased by > 4x with increased T_g, but their shallow energetic positions relative to the valence band undermine their effectiveness as NRCs. [E_c – 2.22 eV] showed the strongest sensitivity to T_g, increasing 5x with reduced T_g, and its deep level formation near the middle of the AlGaN band gap is consistent with an active NRC. However, the comparatively low [E_c – 2.22 eV] – ~15x less than [E_c – 2.80 eV] and ~5x less than [E_c – 3.30 eV/E_c – 3.50 eV] for T_g = 1010 ºC – suggests a relatively weak influence of the E_c – 2.22 eV on τ_{nr}. Conversely, the E_c – 2.80 eV deep level is a likely candidate for the dominant NRC, as it had the largest N_t for both T_g values and evidenced a large reduction in N_t with increasing T_g. Identifying the E_c – 2.80 eV defect state as an effective NRC is consistent with its aforementioned similarity to deep levels associated with V_{III} in AlGaN, which is suspected to be the dominant NRC in AlGaN MQWs.[6]

In conclusion, the influence of MQW region T_g on AlGaN/(Al)GaN MQW PL and point defect incorporation was investigated. Band edge PL intensity from MQWs emitting at ~ 340 nm increased by a factor of > 4x when T_g was increased from 1010 ºC to 1060 ºC. DLOS was used to monitor the influence of T_g on defect incorporation in AlGaN epilayers grown under nominal QW region growth conditions. While the types of defect levels did not change as T_g was increased from 1010 ºC to 1060 ºC, the individual and overall N_t increased by ~ 4x. A deep level defect at E_c – 2.80 eV was tentatively attributed to a V_{III}-related defect and suggested to be the

dominant NRC. Regardless of which particular deep level most degrades PL intensity, this study demonstrates that T_g of the MQW region can critically impact optical efficiency by controlling defect incorporation. Optimization of MQW region T_g is expected to have corresponding importance to achieving highly efficiency AlGaN-based UV LEDs and LDs.

3.3 Development of p-type short-period superlattices

Because the acceptor ionization energies increase rapidly with increasing Al composition, demonstrating room temperature p-type conductivity in these Al-rich $Al_xGa_{1-x}N$ alloys has been difficult. Li *et al.* report an activation energy exceeding 300 meV in $Al_xGa_{1-x}N$ epilayers where the Al concentration approaches only 0.30.[16] One promising approach to circumventing these high activation energies is the application of superlattice (SL) structures typically consisting of GaN and $Al_xGa_{1-x}N$ alloys doped with Mg. As first proposed by Schubert *et al.*[17], the compositional modulation of superlattices grown on the c-plane induces polarization fields leading to enhanced ionization of acceptors. Several reports of enhanced hole concentrations (exceeding $1x10^{18}cm^{-3}$) in Mg-doped GaN-$Al_xGa_{1-x}N$ SL structures grown by metal-organic vapor phase epitaxy have been published.[18-20] These SLs typically have a period of 50-300 Å and have an average Al composition of 0.40 or less. While the bandgap remains too low for deep-UV applications, these GaN-$Al_xGa_{1-x}N$ SLs have proven effective as p-cladding layers in InGaN laser diodes in the near-UV and blue region.[21]

In further studies, Nikishin and co-workers have extended the concept of Mg-doped SLs to significantly higher Al compositions.[22-25] Unlike previous work, they employed gas-source molecular beam epitaxy (GS-MBE) to fabricate short-period superlattice (SPSL) structures consisting of monolayer thick layers of AlN and $Al_xGa_{1-x}N$ with a large difference in Al-composition (>0.90) between epilayers. They reported P-type conductivity in Mg-doped SPSL structures consisting of 7.5-15 Å thick AlN barrier layers and 5-7.5 Å thick $Al_xGa_{1-x}N$ ($0.05 < x < 0.10$) well layers. They also reported a hole concentration of $1x10^{18}$ cm^{-3} and a resistivity of 6 ohm-cm for a SL with an average Al composition of 0.72. Electroluminescence down to 250 nm from LEDs incorporating Mg-doped SLs was demonstrated as well.

These promising GS-MBE results have led us to investigate the growth of Mg-doped short-period superlattice (Mg-SPSL) structures at high Al compositions using metal-organic vapor phase epitaxy (MOVPE). Here, we report on electrical, optical, and structural properties of Mg-SPSL structures with bandgaps suitable for p-type optical cladding layers in deep-UV lasers diodes. This work encompasses a range of AlN/$Al_xGa_{1-x}N$ SPSL structures grown on various $Al_xGa_{1-x}N$ templates and extends the range of MOVPE-grown p-type Mg-SPSL structures to 0.74**.**

Superlattices were grown using MOVPE in a Veeco D-125 reactor. Conventional precursors, including trimethylgallium (TMGa), trimethylaluminum (TMAl), and ammonia, were used to grow $Al_xGa_{1-x}N$ alloys, and silane and bis(cyclopentadienyl)magnesium (Cp_2Mg) were used as dopant sources. Nitrogen and hydrogen were used as carrier gases. Growth was performed at a pressure of 75 torr and a temperature of 1010°C as measured by pyrometers. $Al_{0.23}Ga_{0.77}N$ well layers were grown at a V/III ratio of 4000, a growth rate of 0.35 μm/hr, and an Al/group-III ratio

of 0.21 while AlN barrier layers were grown at a V/III ratio of 5000 and a growth rate of 0.10 μm/hr. There were no growth interruptions between layers, and for p-type growths, a constant Mg flux was maintained to the chamber during growth. Following growth, Mg-SPSL samples were thermally annealed at 900ºC for five minutes under nitrogen to activate Mg dopants.

The starting growth templates were previously prepared, 1.5 μm-thick, AlN epilayers grown on (0001) c-plane sapphire substrates mis-oriented 0.2° toward the m-plane. The dislocation density of the AlN templates varied from 4-8 x 10^9 cm^{-2} as determined from x-ray diffraction measurements.[26] We did not observe a significant correlation between resistivity of Mg-SPSLs and the dislocation density of the AlN template. A few growths employed templates consisting of a 0.75 μm thick, undoped $Al_{0.61}Ga_{0.39}N$ epilayer grown on 1.5 μm of AlN on sapphire. The dislocation density of the $Al_{0.61}Ga_{0.39}N$ templates is similar to that of the underling AlN epilayer. The resistivity of Mg-SPSLs on templates near this Al composition range is of particular interest since this approximates the structure of a ~ 280 nm laser diode where the Mg-SPSL, serving as the p-cladding, would be grown on an n-cladding layer of $Al_xGa_{1-x}N$ where x ~ 0.60 .

The regrown SPSL structures consisted of alternating $Al_{0.23}Ga_{0.77}N$ well and AlN barrier layers where the period was varied from 10-25 Å by changing the thicknesses of the well and/or barrier layers from 5-15 Å. The total thickness of the superlattices varied from 0.03-1.1 μm although the majority of samples were 0.3-0.5 μm thick. All Mg-doped SPSLs were capped with a 20 Å thick, Mg-doped $Al_{0.23}Ga_{0.77}N$ contact layer.

The chosen composition of the well layers was a compromise between higher average SL compositions and bandgaps (for higher well compositions) versus lower hole resistivities and greater strains in the wells (for lower well compositions). To aid in the selection of the well-layer Al composition, we investigated growth conditions which minimize hole resistivity of Mg-doped $Al_xGa_{1-x}N$ epilayers ($0.10 < x < 0.30$). A relatively small increase in resistivity, from 1-2 ohm-cm to 2-4 ohm-cm, was observed in $Al_xGa_{1-x}N$ epilayers when the Al composition was increased from 0.10 to 0.23. Hole concentrations of 5-9 x 10^{17} cm^{-3}, mobilities of 3.9-3.3 cm^2/Vs, and resistivities of 3.3-2.1 ohm-cm were measured for Mg- doped $Al_{0.23}Ga_{0.77}N$ epilayers reproducibly grown during the course of this study. In contrast, significantly higher resistivities of 8-13 ohm-cm were measured when Al compositions were increased to 0.30. Consequently, an Al composition of 0.23 was selected for the well layers; in the resulting superlattices, the resistivity is only moderately higher than in p-GaN; and there is a large difference in Al-composition (>0.75) between well and barrier layers. Additionally, SLs with $Al_{0.23}Ga_{0.77}N$ wells and AlN barriers of equal thickness have an average composition of 0.62 which is suitable for a p-type cladding layer in a laser diode with emission near 280 nm.

The hole concentration, mobility, and lateral resistivity were measured at room temperature with Hall measurements using the van der Pauw method. Since Hall measurements made on an undoped SPSL before and after thermal annealing were insulating, we can conclude that Mg in the SPSL is responsible for hole conduction. While hole concentrations and mobilities were often inconsistent with current, resistivity measurements were reproducibly within 5% over the range of currents utilized. For convenience, contacts were usually made by pressing preformed indium balls. This approach yielded the same resistivity as seen for 0.6 μm thick Mg-SPSL reference samples prepared with evaporated Pd/Au (200 Å / 1200 Å) contacts that were

thermally annealed under nitrogen at 500°C for 60 seconds. To further validate the use of pressed Indium for contacts, a similar reference sample was grown and capped with a 0.5 μm thick p-GaN contact layer. After fabricating Pd/Au contacts, the exposed p-GaN layer was etched away and subsequent resistivity measurements were again in agreement with those for Indium contacts. The constant resistivities observed for the various contacting schemes suggest that interface resistances are not dominating the measured p-type resistivities.

To determine the effective bandgap and to assess the transmission properties of SPSL structures, optical reflectance and transmission measurements were made with a CARY 300 spectrophotometer system. X-ray diffraction measurements were performed using a Philips X'Pert Pro diffractometer equipped with a hybrid monochromator delivering Cu $K\alpha_1$ x-rays and an asymmetric (220) Ge diffracted-beam analyzer. Omega-2theta scans about the (00.2) reflection were used to determine the average composition and period of superlattices. Dynamical diffraction simulations calculated using the Philips X'Pert Epitaxy program were compared to the measured scans to confirm the composition and period of the SPSL.

Since growth temperature and group-III/Mg ratio were found to be important in minimizing the hole resistivity of $Al_xGa_{1-x}N$ epilayers ($0.10 < x < 0.30$), we investigated the lateral resistivity of Mg-SPSL structures as a function of these same two growth parameters. Figure 12 (a) shows the room-temperature resistivity as a function of growth temperature for 0.3 μm thick superlattices with an average Al composition of 0.62, where the barrier and the well layers are each 5 Å thick. For a group-III/Mg ratio of 734, a minimum resistivity of 7-9 ohm-cm is reproducibly achieved for Mg-SPSL structures grown at 990-1010°C. For comparison, Figure 12 (a) also shows the resistivity of 0.5 μm thick, Mg-doped, $Al_{0.23}Ga_{0.77}N$ epilayers. We observe that the growth temperature that minimizes resistivity for Mg-SPSLs is nearly the same as that found for p-type $Al_{0.23}Ga_{0.77}N$ epilayers.

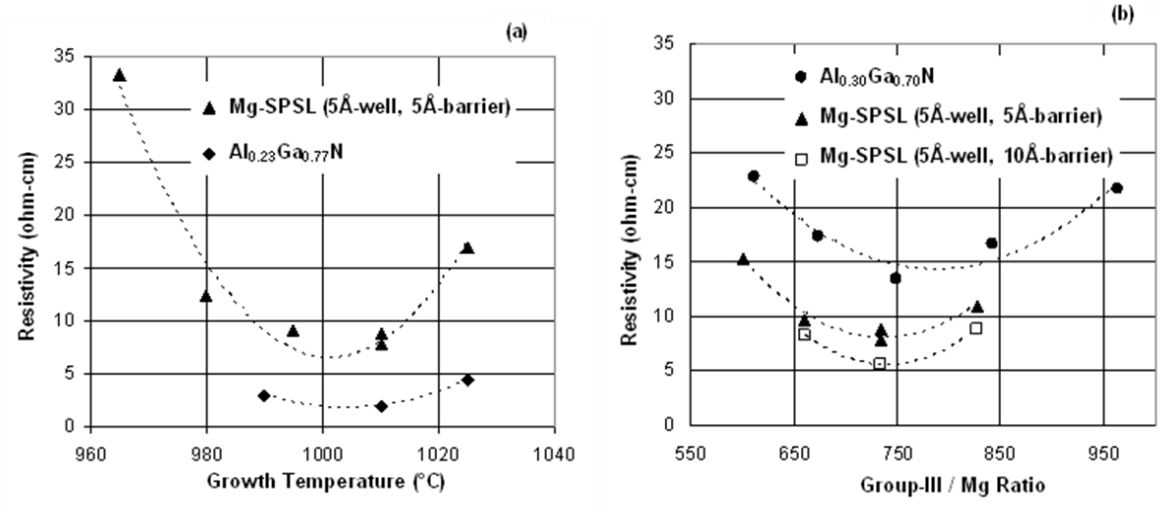

Figure 12: Room-temperature p-type resistivity of Mg-SPSL and AlGaN epilayer samples as a function of (a) growth temperature and (b) group-III / Mg ratio of the $Al_{0.30}Ga_{0.70}N$ epilayer or the $Al_{0.23}Ga_{0.77}N$ well layer in Mg-SPSL structures. Samples are grown on AlN-sapphire templates (filled) or on $Al_{0.61}Ga_{0.39}N$-AlN-sapphire templates (open). The dashed lines are provided as guides to the eye.

Figure 12(b) shows the dependence of lateral resistivity on the group-III/Mg ratio of the well layer for superlattices structures with 5 Å well layers and 5 Å or 10 Å barrier layers for structures all grown at 1010°C. For both Mg-SPSL structures, we note that the resistivity is particularly sensitive to Mg flow and minimized at the same group-III/Mg ratio of 734. Also shown in Figure 12b is the resistivity of 0.5 μm thick Mg-doped $Al_{0.30}Ga_{0.70}N$ epilayers as a function of group-III/Mg ratio. Though not shown, we observed a similar resistivity trend for $Al_{0.23}Ga_{0.77}N$ epilayers. As with growth temperature, we find the Mg flux that minimizes the resistivity of $Al_xGa_{1-x}N$ epilayers also minimizes the resistivity of Mg-SPSLs. We speculate that these coincident minima result because the Mg concentration reaches a fixed upper limit prior to the formation of self-compensating defects.

To evaluate the plausibility of self-compensation and evaluate overall Mg incorporation, secondary ion mass spectroscopy (SIMS) was used to measure the Mg concentration in a series of $Al_xGa_{1-x}N$ epilayers and a Mg-SPSL consisting of well and barrier layers each 10 Å thick (see Table 1). For each sample, growth conditions and Mg flux were optimized to minimize resistivity. Regardless of the composition, the resistivities of $Al_xGa_{1-x}N$ epilayers ($0 < x < 0.3$) were minimized at a common Mg concentration near 4×10^{19} cm^{-3}. For the Mg-SPSL sample, the Mg flux that minimized the resistivity of Mg-SPSL was employed during both $Al_{0.23}Ga_{0.7}N$ well and AlN barrier layers. From Table 1, we see that this approach yielded an average Mg concentration of 2.7×10^{19} cm^{-3}. Given the anticipated 4×10^{19} cm^{-3} Mg concentration in the well layer, this suggests that the Mg concentration in the AlN barrier is 1.4×10^{19} cm^{-3}. However, a Mg concentration near 4×10^{19} cm^{-3} was measured in a Mg-doped AlN epilayer grown under the same conditions as the barrier layers. The discrepancy in the Mg concentration in the AlN barrier is possibly related to uncertainty in the SIMS measurements of these high Al composition materials; alternatively, transient phenomenon associated with short-period superlattice growth may alter overall Mg incorporation. In any case, we can conclude that an appreciable level ($> 1 \times 10^{19}$ cm^{-3}) of Mg was incorporated into the AlN barrier layers in the Mg-SPSL.

Table 1: Mg concentration and resistivity of $Al_xGa_{1-x}N$ epilayers and a Mg-SPSL with 10 Å $Al_{0.23}Ga_{0.77}N$ well and 10 Å AlN barrier layers.

Material	[Mg] cm-3	Resistivity (ohm-cm)
GaN	3.8×10^{19}	0.8
$Al_{0.23}Ga_{0.77}N$	3.7×10^{19}	2.1
$Al_{0.30}Ga_{0.70}N$	4.2×10^{19}	10.5
AlN	4.4×10^{19}	Not measured
Mg-SPSL	2.7×10^{19}	8

Guided by initial process window found in Figure 12 experiments, we next investigated the resistivity of Mg-SPSLs as a function of average Al composition. As shown in Figure 13 the Al composition was varied from 0.42 to 0.74 by changing the width of the $Al_{0.23}Ga_{0.77}N$ well layers from 5-15 Å in SPSL structures with either 5 Å or 10 Å AlN barriers. P-type lateral resistivities less than 10 ohm-cm were measured for Mg-SPSLs with an average Al composition from 0.42 to 0.74 for growths on both AlN and $Al_{0.61}Ga_{0.39}N$ templates. Most notably, a p-type lateral

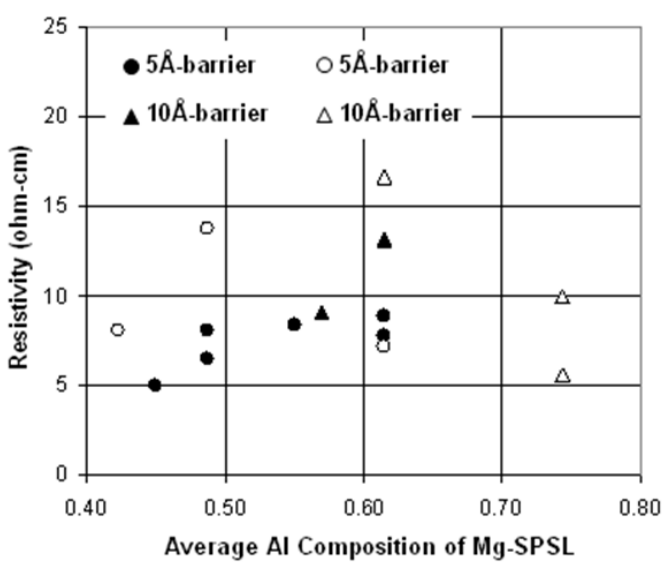

Figure 13: Resistivity of Mg-SPSL structures consisting of $Al_{0.23}Ga_{0.77}N$ wells and either 5 Å (circles) or 10Å (triangles) AlN barriers. Resistivities less than 10 ohm-cm were measured in Mg-SPSL grown on both AlN-sapphire templates (filled) or on $Al_{0.61}Ga_{0.39}N$-AlN-sapphire templates (open).

resistivity of 6 ohm-cm was measured in a Mg-SPSL structure with an average Al composition of 0.74 grown on an $Al_{0.61}Ga_{0.39}N$ template. The lateral resistivities reported in this work are an upper limit since current is assumed to be uniformly distributed over the full thickness of the SL. Depending on the relative magnitude of the vertical resistance, only a fraction of the total thickness of the SL might be conducting, and the lateral resistivity could thus be significantly lower. We note in Figure 13 that the resistivity can vary for Mg-SPSLs of the same structure but grown on different templates. We suspect that the strain state of the template could be responsible for the different resistivities; this possibility is under investigation.

In further studies, we verified that current leakage in the SPSLs due to vertical threading dislocations is negligible since Hall measurements indicated that an undoped SPSL grown on a Si-doped, conducting, (N_o = 5 x 10^{17} m^{-3}, μ = 20 cm^2/Vs) SPSL was insulating. If vertical current leakage had been significant, the conductivity of the underlying, Si-doped SPSL would have been detected in the Hall measurements.

To assess hole concentration, mobility, resistivity, and activation energy, room temperature Hall measurements were made. Only a limited number of samples yield meaningful Hall measurements of hole concentration and mobility. For these samples, hole concentrations of 1-10 x 10^{17} cm^{-3} and mobilities of 0.4 to 4 cm^2/Vs were measured. This range of hole concentration is similar to that reported by Nikishin.[24] For selected samples, Hall measurements

were made as a function of temperature to investigate the ionization energy of Mg acceptors in SPSL structures. Since hole concentrations were not reliably measured over the temperature range investigated, we show in Figure 14(a) temperature dependent resistivity data for two Mg-SPSLs and a p-GaN epilayer. One Mg-SPSL consisted of well and barrier layers each 5 Å thick giving an average Al composition of 0.62, and contacts were made using pressed Indium. The other Mg-SPSL consisted of 10 Å well and 5 Å barrier layers resulting in an average composition of 0.49; this sample, as well as the p-GaN epilayer, had Pd / Au contacts. The resistivity of the p-GaN increased quickly at lower temperatures as expected and was too high to measure below 180K. However, we observe a much weaker dependence of resistivity on temperature for the two Mg-SPSL samples. Assuming the mobility is slowly varying with temperature, the acceptor ionization energy can be extracted from the slope of the log plot of resistivity versus the inverse of temperature. Accordingly, in Figure 14(b) we analyze the temperature dependent resistivity in an Arrhenius Plot and find an activation energy of 150 meV for Mg acceptors in p-GaN. This is consistent with the 157 meV reported by Tanaka for p-GaN.[27] In marked contrast, we measure activation energies of only 29 meV and 18 meV in the Mg-SPSLs with average compositions of 0.62 and 0.40. It is interesting to note that Kumakura[28] reports an activation energy of 20.5 meV for a GaN-$Al_{0.40}Ga_{0.60}N$ (50Å/50Å) superlattice with an average composition of 0.40. We see a similar activation energy (18 meV) in our Mg-SPSL with a slightly higher Al composition (0.49) and a period of only 15 Å.

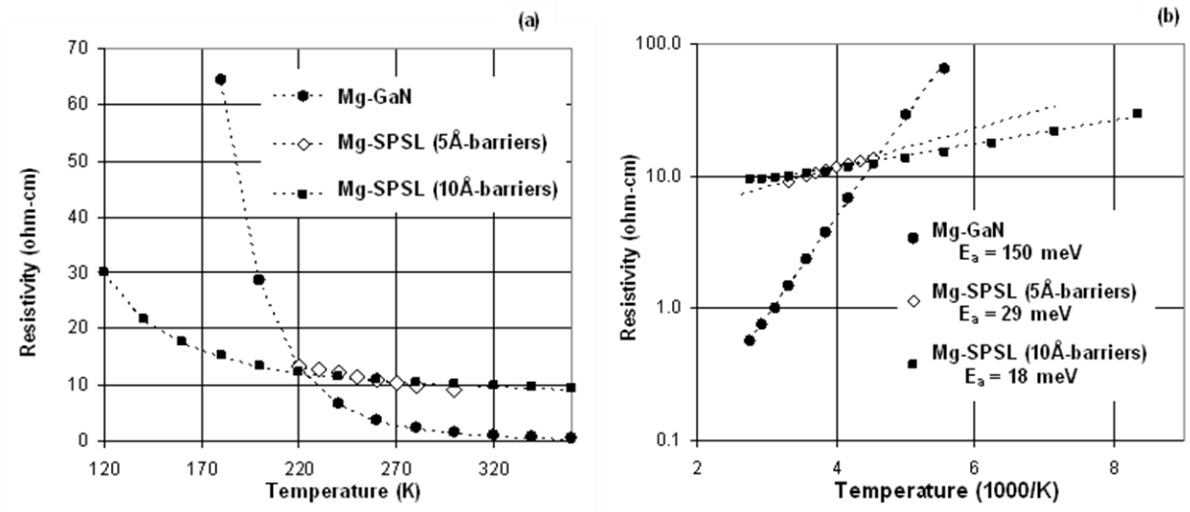

Figure 14: Resistivity vs (a) temperature and (b) inverse of temperature for p-GaN (circles), and a Mg-SPSL with 5 Å AlN barriers and 5 Å (diamonds) or 10 Å (squares) $Al_{0.23}Ga_{0.77}N$ well layers. Dashed lines in (a) are guides to the eye and in (b) are fits to the data using an Arrhenius model.

Optical reflectance and transmission measurements of Mg-SPSL structures were made to assess the effective optical bandgap and evaluate transmission properties. Figure 15(a) shows the optical reflectance and derivative spectra for a 0.3 μm thick Mg-SPSL with an average Al composition of 0.62 where the barrier and well layers are each 10 Å thick. The effective optical bandgap is determined from the spectral position of the damping of Fabry-Perot interference fringes in the reflectance spectrum, signifying increasing absorption of the incident light. The spectra shows the sample to be transparent to wavelengths longer than approximately 249 nm.

This corresponds to an optical bandgap of 5.0 eV, which is equivalent to the bandgap of a random $Al_xGa_{1-x}N$ alloy with an Al composition of 0.62. Changes in the well or barrier thickness resulted in corresponding shifts in the optical bandgap indicating that the average Al composition of the Mg-SPSL changed in response to changes in the SPSL structure. By changing either the well or barriers thickness to either 5 or 10 Å, SPSLs could be grown with an effective optical bandgap equivalent to $Al_xGa_{1-x}N$ alloys with an Al composition ranging from 0.49 to 0.74.

Optical transmission measurements in a single-pass geometry were used to confirm effective bandgap energies determined from reflectance measurements. In Figure 15(b), optical transmission spectra are shown for an AlN-on-sapphire template typical of that used in this study; for a 0.3 μm-thick, Mg-doped, $Al_{0.61}Ga_{0.39}N$ epilayer; and for two different 0.3 μm-thick Mg-SPSL structures. All of the samples in Figure 15(b) were grown on sapphire wafers where both sides had been polished prior to growth. Both Mg-SPSL structures have an average Al composition of 0.62 but differing periods (10 Å and 20 Å). The data demonstrate that Mg-SPSL structures with wells up to 10 Å thick approximate the transmission properties of a random alloy of the same composition. More sophisticated measurements are needed to quantify below-bandgap optical losses in Mg-SPSL structures to determine their suitability for a p-cladding layer in laser diodes.

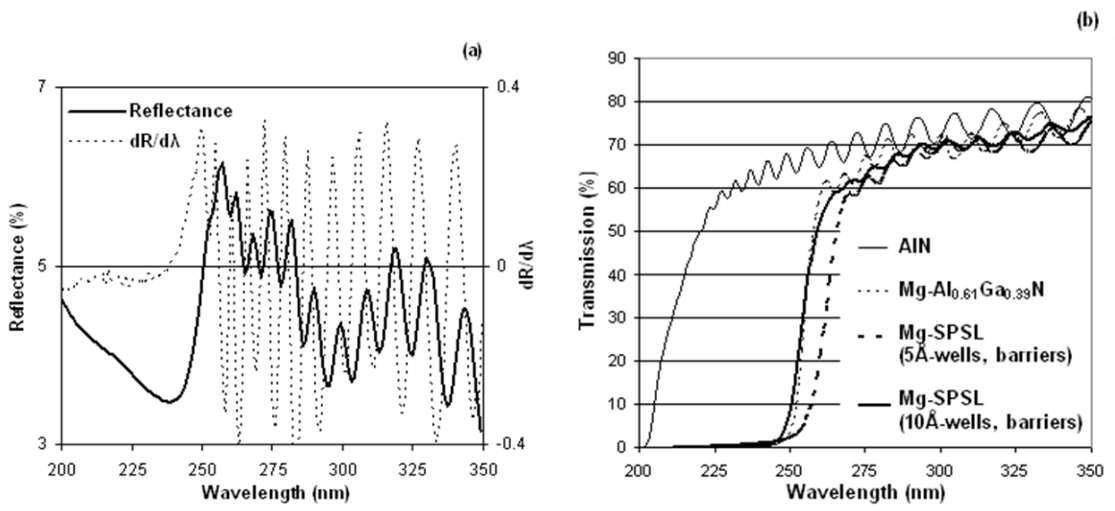

Figure 15: (a) Optical reflectance and derivative spectra for a Mg-SPSL with barrier and well layers each 10 Å thick. (b) Transmission spectra for an AlN-on-sapphire template, a Mg-doped $Al_{0.61}Ga_{0.39}N$ epilayer, and two Mg-SPSL structures with an average Al composition of 0.62.

X-ray diffraction measurements were used to determine the period and average composition of SPSL structures. Figure 16 shows omega-2theta scans about the (00.2) reflection from a Mg-doped and undoped SPSL, both consisting of 10 Å well and barrier layers. Both samples were annealed post-growth at 900°C for five minutes to replicate a typical Mg activation process. In the scan from the undoped SPSL, the n = +/-1 satellite peaks are well resolved and the n = -2 peak, while broader, is discernable. However, only a much weaker n = -1 peak is observed in the Mg-SPSL suggesting that the interfaces of the SPSL are degraded when the structure is doped with Mg. While not shown, an x-ray scan of a Si-doped SPSL with 10 Å well and barrier

layers is nearly identical to that from the undoped SPSL. The combined results suggest that the properties of Mg on the growth surface are likely responsible for the degradation in satellite peaks measured in the Mg-SPSL structure.

No change in the average composition occurred in SPSL structures with Mg-doping or after thermal annealing since no shift in the n = 0 superlattice-satellite peak was observed. The measured average Al composition for the Mg-SPSL in Figure 16 is 0.61 in agreement with the calibrated target value of 0.62 for the structure. The measured period of the undoped SPSL is 17.4 Å or 13 percent less than the targeted period of 20 Å. Since the growth times for well and barrier layers were determined from thick calibration layers using an *in-situ* reflectance monitor, this relatively small difference is unsurprising.

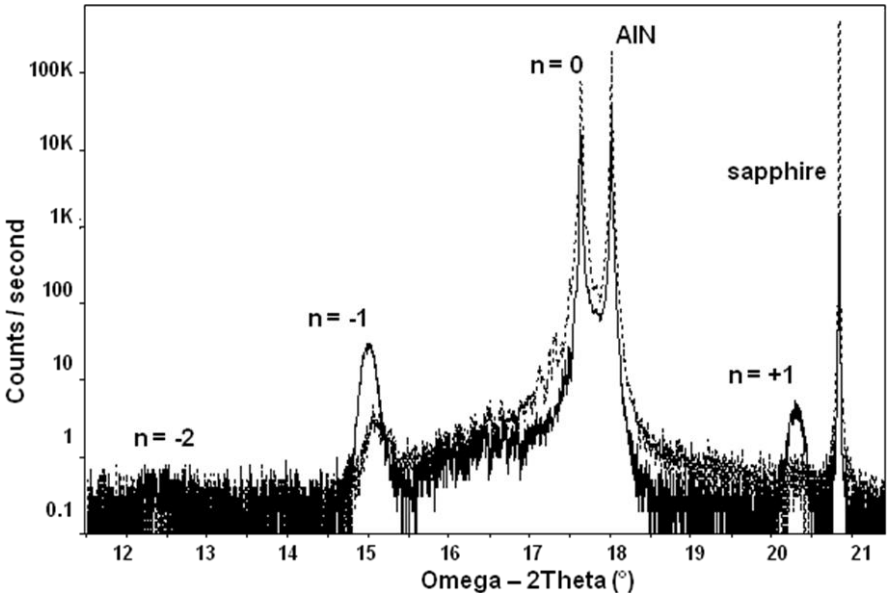

Figure 16: Omega-2theta x-ray diffraction (XRD) scans about the (0002) reflection for Mg-doped (dashed) and undoped (solid) SPSLs with $Al_{0.23}Ga_{0.77}N$ well and AlN barrier layers each 10 Å thick.

While not shown, x-ray diffraction scans of Si-doped SPSLs consisting of 5 Å well and barrier layers showed only the n = -1 satellite peak. When Mg was introduced only during growth of the well, the n = -1 satellite peak was weaker and broader; this satellite peak vanished altogether in scans of samples where Mg was in both the well and barrier layers. No lateral conductivity was measured in the sample where Mg was only introduced into the well layer while a resistivity of 8 ohm-cm was measured in the sample when both the well and barrier layers were doped at the optimum group-III/Mg ratio of 734. The reduction in resistivity might not be related to the degradation of the interface with increasing Mg since we observe increasing resistivities at higher group-III/Mg ratios (Figure 13) where presumably the interfaces would be further degraded with higher levels of Mg doping.

In summary, we report the MOVPE growth and characterization of Mg-doped short-period superlattices consisting of nm-thick layers of AlN and $Al_{0.23}Ga_{0.77}N$. Optical reflectance and transmission measurements demonstrated that Mg-SPSLs with periods of 20 Å or less have an optical transparency similar to random-alloy $Al_xGa_{1-x}N$ epilayers of the same average

composition. X-ray diffraction measurements confirmed that the period and average Al composition of the Mg-SPSL are in reasonable agreement with targeted values. Additionally, we found that Mg-doping of SPSL structures degraded or eliminated satellite peaks that were observed in XRD scans of undoped or Si-doped SPSL structures. This result suggests that the presence of Mg during growth roughens the growing surface and the epilayer interfaces. The growth temperature (1010 °C) and group-III/Mg ratio (734) that minimized resistivity of $Al_{0.23}Ga_{0.77}N$ epilayers also minimized the lateral, p-type resistivity of Mg-SPSL structures in which $Al_{0.23}Ga_{0.77}N$ was used as the well layer. P-type resistivities of less than 10 ohm-cm were achieved for Mg-SPSL with an average Al composition from 0.42 to 0.74. We report a resistivity of 6 ohm-cm in a superlattice with an average Al composition of 0.74 grown on an $Al_{0.61}Ga_{0.39}N$ template. Using the temperature dependence of resistivity, we determined an activation energy of 29 meV in a Mg-SPSL with an average composition of 0.62 and 18 meV for a Mg-SPSL with a composition of 0.49.

Overall, we observe similar optical properties and p-type resistivities in Mg-SPSL grown by MOVPE as Mg-SPSLs grown by Nikishin *et. al.* using GS-MBE.[24] This work extends the range of AlGaN based Mg-SL structures grown by MOVPE that exhibit hole conduction to Al compositions of 0.74, which is a suitable composition for cladding layers in ~280 nm laser diode structures. Further studies to quantitatively assess vertical transport properties and optical losses in Mg-SPSL will more clearly delineate the potential of these structures for vertical injection deep-UV optoelectronic devices.

4. ALGAN LASER DIODE DEVELOPMENT

4.1 Laser design

The primary laser design that we used in this project was a ridge waveguide structure, similar to that shown in Figure 17. Our designs encompassed ridge widths from 2-7 μm and cavity lengths from 0.5-1.5 mm. The fabrication process employed Cl_2-based ICP etching to define the laser facet, the laser ridge and finally a "mesa" etch through the active layers to gain access to the n-contact layer. As such, much of the processing was fairly standard for AlGaN devices, including LEDs[1] with the exception of the laser facet process. We therefore focus below on a detailed description of our efforts to achieve high quality laser facets in AlGaN.

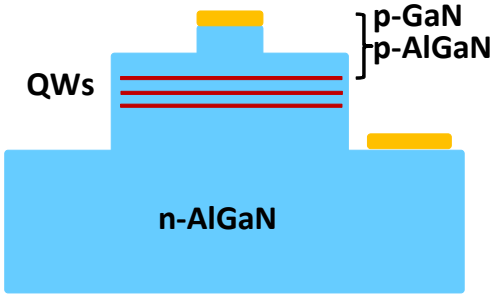

Figure 17: Schematic of AlGaN ridge waveguide laser design (not to scale)

4.2 Processes for high quality etched facets

Of great importance is the minimization of laser cavity loss through fabrication of highly smooth and vertical laser facets. In this section, we describe a process for the fabrication of low-loss etched laser facets that is applicable to deep-UV $Al_xGa_{1-x}N$ laser heterostructures where the composition ranges from x=0-0.5 and possibly higher.

To date, several methods have been employed to fabricate facets for GaN-based near-UV lasers including cleaving,[29,30] milling with focused ion beams (FIB),[31,32] plasma etching,[33-35] chemically assisted ion beam etching,[36,37] and two-step processes combining plasma etching or photo-enhanced electrochemical etching with wet chemical etching.[38-42] Of these methods, cleaving has produced the smoothest facet surfaces with root mean square (RMS) roughness values on the order of 1 nm for GaN-based laser diodes (LDs) grown on SiC.[30] However, etched facets have a number of advantages, including applicability to laser epilayers grown on substrates such as sapphire, that do not have common cleavage planes, and the potential for on-wafer laser testing. Careful manipulation of plasma-etching parameters have led to GaN-based laser facets with RMS roughness values on the order of 20 nm[5] and facet angles ranging from 5° to 1° from vertical.[31,33] Further improvements to plasma-etched facets have been achieved with subsequent wet chemical etching using KOH-based solutions that reveal particular crystallographic planes.[39] In the work reported here, we advance this two-step method by optimizing both inductively-coupled plasma (ICP) etching and wet-etching parameters and demonstrating applicability to $Al_xGa_{1-x}N$-based deep-UV laser structures comprising a wide compositional range.

The processing of laser facets was studied using two different heterostructures, both grown by MOVPE on c-plane sapphire. The first sample has a separate confinement heterostructure laser design suitable for emission at 340 nm and includes n-type and p-type $Al_{0.3}Ga_{0.7}N$ cladding layers, $Al_{0.22}Ga_{0.8}N$ waveguide layers, a $GaN/Al_{0.22}Ga_{0.8}N$ quantum well active region, an

$Al_{0.5}Ga_{0.5}N$ electron block layer and a p-GaN cap layer. The second sample is an undoped 4 μm thick $Al_{0.3}Ga_{0.7}N$ epilayer which serves as a simplified reference sample. To fabricate test facets for laser development, a hard mask was formed by depositing 1 μm of SiO_2 by plasma-enhanced chemical vapor deposition. The mask was then patterned into stripes aligned in the <1-120> direction. Although complete laser diode devices were not fabricated here, the stripe sidewalls represent the laser facets and embody the (10-10) plane of the AlGaN heterostructure. Plasma etching of the AlGaN material was performed by ICP etching with a $Cl_2/BCl_3/Ar$ (16/4/5 sccm) chemistry. All samples were etched to a depth of 3 μm, which corresponds to 0.9 μm into the n-type cladding layer of the laser structure. The surface roughness of the resulting (10-10) laser facets was characterized using atomic force microscopy (AFM) on samples cleaved along the stripe direction to provide access to the facet surface. Further characterization of the facet morphology and profile was provided by cross-sectional scanning electron microscope (SEM) images of samples cleaved in a direction perpendicular to the stripes.

Optimization of the plasma-etching process for the AlGaN laser structure was achieved by varying the substrate rf power and the chuck temperature, while the ICP power and pressure were held constant at 125W and 2 mT, respectively. In Table 2, we summarize the achieved facet angles as a function of chuck temperature and rf power. Our studies reveal that temperature strongly influences facet angle. By holding the rf power at a constant value of 250W and increasing the temperature from 20°C to 180°C, the facet angle decreased from 8° to 5°. Notably, varying the rf power from 50W to 250W had little impact on the facet angle, either at 20°C or 180°C. Only the lowest power studied (10W, 20°C) yielded a significantly larger angle of 12°. Instead, increasing the rf power led to both an increased etch rate and decreased etch selectivity between the AlGaN and the oxide mask (Table 2). Our studies also showed that the extent of microtrenching (a trench formed along the bottom of the facet where it intersects with the c-plane material) systematically decreased with increasing rf power at 180°C, becoming much less evident at 250W. These observations suggest that optimal plasma-etching conditions include both higher temperatures and higher rf powers. The maximum accessible temperature of 180°C and rf power of 250W produced one of the best facet angles, approximately 5°, with minimal microtrenching, as shown in Figure 18.

Table 2: Results of plasma etching studies of AlGaN laser structures, including facet angles referenced from surface normal, etch rates, and etch selectivity between AlGaN material and oxide mask as a function of rf power and temperature.

Rf power (W)	Temp (°C)	Facet Angle (°)	Etch Rate (Å/min)	Selectivity (AlGaN /Oxide)
10	20	12	860	6.4
50	20	7	2520	9
50	180	5.1	2820	7.5
150	180	5.2	4160	6.5
250	20	8	4790	8.8
250	50	6.3	4700	8
250	100	6.4	4650	6.6
250	150	5.5	4720	6.3
250	180	5.2	4660	6.3

The SEM micrograph in Figure 18 also shows that the defining edge of the oxide mask becomes rounded during plasma etching. The sloping of the sharp mask edge as well as the vertical striations in the oxide mask likely caused roughening of the adjacent facet during plasma etching. AFM measurements reveal that the RMS roughness was not uniform and ranged from 1.4 nm to 20 nm, from the top to the bottom of the facet. Both the facet tilt[43,44] and facet roughness[29] can significantly degrade the reflectivity from that of a perfectly smooth and vertical AlGaN/air interface. For the plasma-etched facet described above, the surface roughness dominates the optical loss. Assuming a refractive index of 2.56 at 340 nm for the $Al_{0.2}Ga_{0.8}N$ waveguide,[45] we find that the 20 nm RMS roughness value reduces the reflectivity to only ~3% of the value for a perfectly smooth facet.[29]

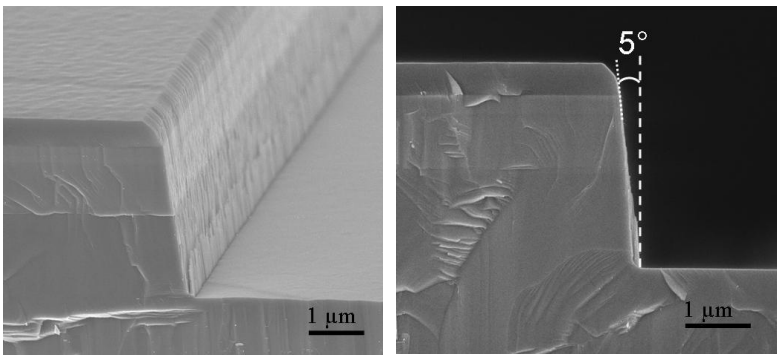

Figure 18: SEM micrographs of the optimized plasma-etched facet achieved in the AlGaN laser structure with an rf power of 250W and a temperature of 180°C. The vertical dashed line is aligned along the crystalline c-axis and represents the desired vertical facet orientation.

To improve facet reflectivity, we next investigated wet chemical etching of the plasma-etched facets. Potassium-hydroxide solutions have been shown to crystallographically etch nitride materials, preferentially exposing the (10-10) and other (10-1n)-type planes via their slow etch rates.[42] Our laser facets parallel the (10-10) plane to take advantage of the selective crystallographic etching in solutions of this type which offers an approach for simultaneously improving the local smoothness and overall orientation of these facets. Initial testing was conducted on $Al_{0.3}Ga_{0.7}N$ epilayers to avoid possible complications from various Al compositions present in the laser structure. The effects of time and temperature of four chemical etchants were tested on the $Al_{0.3}Ga_{0.7}N$ epilayers which were first plasma etched with the previously optimized rf power (250W) and chuck temperature (180°C). The different chemical treatments included 10% by weight KOH in ethylene glycol, the KOH-based photoresist developers AZ400K and AZ421K (AZ Electronic Materials USA Corp.), and tetramethylammonium hydroxide. Of those solutions tested, the AZ400K developer at 80°C provided the best results for $Al_{0.3}Ga_{0.7}N$ epilayer facets. Exposure for 20 minutes improved the $Al_{0.3}Ga_{0.7}N$ facet angle from 4° after plasma etching to less than 2° and resulted in a visibly smoother surface. Based on these results, etching studies on the AlGaN laser structure were then carried out in the AZ400K developer at 80°C.

Wet etch studies of plasma-etched laser facets examined two important issues. The first issue is whether the difference in etch rates of the various compositions of AlGaN might be sufficient to cause horizontal striations in the otherwise smooth facet surface. The second issue is whether optimization of plasma-etching conditions was necessary, given the marked improvements attainable by subsequent wet chemical etching of the $Al_{0.3}Ga_{0.7}N$ facets. Our studies employed four AlGaN laser structure samples processed with different ICP etch conditions and treated in AZ400K developer at 80°C for 5, 10 and 20 minutes. The AlGaN laser structures were plasma etched with rf powers and chuck temperatures of 250W-180°C, 250W-20°C, 50W-180°C and 10W-20°C corresponding to plasma-etched facet angles of 5.2°, 8°, 5.1°, and 12°, respectively. This range of initial facet angles would determine the efficacy of the wet chemical etches, and observations of the sidewall would indicate whether preferential etching had occurred.

Of these treatments, the 250W-180°C sample treated for 20 minutes with AZ400K at 80°C produced the best results (Figure 19a). This treatment yielded an average facet angle of 0.7° from vertical and an RMS roughness of only 1.1 nm over a 1x1 μm^2 area. Slightly larger scans, up to 3x3 μm^2, indicated a roughness value less than 2 nm. As shown in Figure 18, no preferential etching of individual layers within the laser structure occurred. The addition of this wet chemical etch results in a facet with an estimated reflectivity exceeding 95% of the ideal reflectivity of the AlGaN/air interface.[2,16] This calculation assumes waveguide and cladding indices of 2.56 and 2.49,[18] respectively, and combines the effect of tilt (0.7°) and roughness (2 nm). The two-step process is thus notably superior to plasma etching alone.

Both the 250W-20°C and 50W-180°C samples also achieved facet angles of less than 1° after 20 minutes of treatment (Figure 19b and 19c). However, microtrenching resulting from the plasma etch conditions was exacerbated by wet chemical etching. The 10W-20°C condition showed incomplete smoothing, and did not become vertical within 20 minutes of treatment (Figure 19d). Longer exposure of up to 40 minutes in the heated AZ400K developer exposed the (10-10) plane, but ultimately led to a non-ideal profile with a 'foot' inclined approximately 32° to the c-

plane. This is likely the (10-13) plane, which is also preferentially exposed by the wet etch, and is not expected to be significantly reduced with longer exposure to the developer.

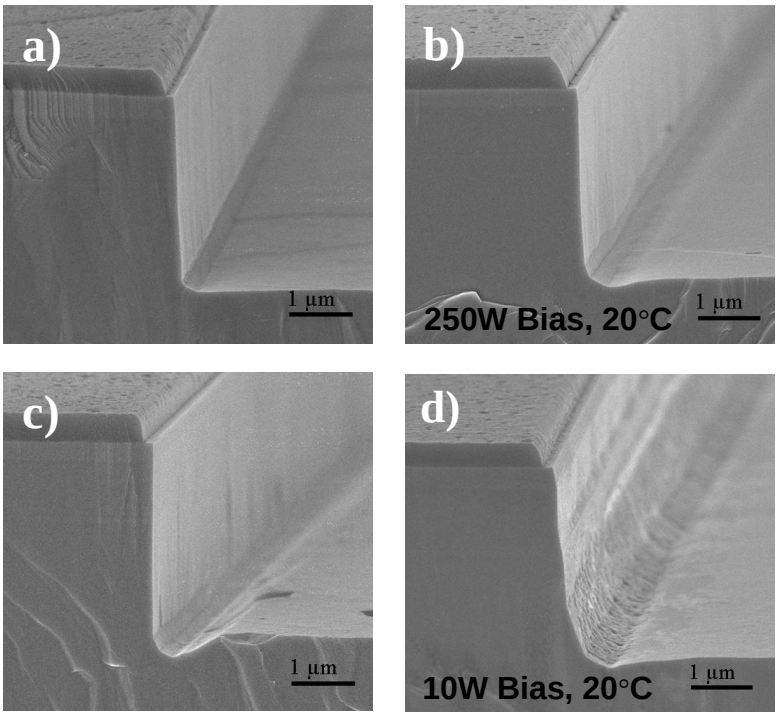

Figure 19: SEM micrographs of facets achieved in AlGaN laser structures using a two-step process of plasma etching and etching in AZ400K developer for 20 minutes at 80°C. The rf powers and temperatures of the plasma-etch process for the various samples were (a) 250W, 180°C, b) 250W, 20°C, c) 50W, 180°C, and d) 10W, 20°C.

Long-term exposure to the AZ400K, necessary for improving non-optimal plasma-etched facets, was found to have several other detrimental effects. For the 10W-20°C sample exposed to the developer for 40 minutes, preferential etching of the p-type GaN layer occurred. Lateral etching of the oxide mask at the top edge of the facet observable after 20 minutes of exposure (Figure 19) was extensive after 40 minutes of exposure. Increased degradation and even perforation of the mask also occurred, potentially leading to preferential etching of defects[42] that could cause shorting in the fully processed laser diode. Overexposure to wet chemical etching can also induce undercutting of the facet due to increased etch rates at the interface of the (10-13) and (10-10) planes. Overall, these observations highlight the importance of achieving sufficient verticality of the original plasma-etched facet to avoid the need for long-term exposure to the AZ400K treatment.

In summary, vertical and smooth facets were demonstrated for deep-UV laser diode structures using a two-step process of ICP etching and wet chemical etching in AZ400K developer. High chuck temperature (180°C) and high rf power (250W) were required to provide plasma-etched facets with a facet angle of 5° and roughness values varying from 1.4 nm to 20 nm. Wet chemical etching in heated (80°C) AZ400K developer was effective in further smoothing and orienting the facet to the (10-10) plane. Combined optimization of plasma-etching and wet-etching conditions led to the formation of a facet with an average sidewall angle of 0.7° from

vertical and less than 2-nm RMS roughness, corresponding to an estimated facet reflectivity greater than 95% of an ideal AlGaN/air interface. No preferential etching was observed for $Al_xGa_{1-x}N$ alloys with compositions in the range x=0-0.5, indicating that this is an effective method to prepare high-reflectivity facets for deep-UV laser diodes.

4.3 Laser Diode Testing

Processed laser bars were packaged and mounted on a temperature controlled stage. Devices with ridge widths between 2-7 microns and cavity lengths of 0.5-1.5 mm were characterized under pulsed current injection. A very low duty cycle of 0.02% was employed to minimize adverse effects of heating. Lasers from one particular wafer run (VNA2723a) achieved very bright electroluminescence and sustained current densities up to 30 kA/cm^2 without degradation. However, to date, none of the laser bars have demonstrated stimulated emission despite the high current densities.

We hypothesize that two factors may be responsible for the lack of stimulated emission. First, it is possible that epitaxial defects are enabling leakage currents that reduce the current density injected into the active layers. Second, the doping profile in waveguide and cladding layers, and particularly p-type layers, may be contributing too much loss, and further optimization is needed.

5. CONCLUSIONS

Through this LDRD project, we made significant strides toward overcoming materials roadblocks to achieving deep UV AlGaN laser diodes. A major focus was on reducing threading dislocations that are non-radiative centers and compromise device reliability. We successfully applied growth over corrugated templates to demonstrate >10x reduction of threading dislocations a >7x enhancement of AlGaN QW PL and a 15x enhancement of electroluminescence. Importantly, this approach was applied over a standard two inch wafer area in contrast to alternative approaches, e.g. use of bulk AlN substrates, that can be limited to much smaller areas.

We also investigated the influence of MQW region growth temperature (T_g) on AlGaN/(Al)GaN point defect incorporation and MQW luminescence efficiency. Band edge PL intensity from MQWs emitting at ~ 340 nm increased by a factor of > 4x when T_g was increased from 1010 ºC to 1060 ºC. Our defect spectroscopy studies of relevant QW epilayers revealed that the types of defect levels did not change as T_g was increased from 1010 ºC to 1060 ºC as three deep levels, found at 2.22 eV, 2.90 eV and 3.30 eV relative to the conduction band, were identified at both growth temperatures. However the individual and overall defect density increased by ~ 4x with the 50°C reduction in growth temperature. This study therefore demonstrated that T_g of the MQW region can critically impact optical efficiency by controlling defect incorporation. Optimization of MQW region T_g is expected to have corresponding importance to achieving highly efficiency AlGaN-based UV LEDs and LDs. Future studies of additional growth parameters, including pressure and V-III ratio, would be valuable to further delineate optimal growth conditions for high luminescence efficiency.

Our approach to circumvent the high acceptor activation energies in AlGaN alloys involved the development of Mg-doped short-period superlattices (Mg-SLs). This work is the first to extend the range of MOVPE-grown AlGaN Mg-SL structures that exhibit hole conduction to Al compositions as high as Al=0.74, which is a suitable composition for cladding layers in ~280 nm LD structures. Further studies to quantify vertical transport properties and optical losses in Mg-SPSL will more clearly delineate the potential of these structures for AlGaN lasers.

We describe our LD fabrication process which enabled ridge waveguide structures over a range of ridge widths and cavity lengths. In particular, we highlighted the development of highly vertical and smooth etched laser facets using a two-step process of ICP etching and wet chemical etching in AZ400K (KOH-based) developer. Combined optimization of plasma-etching and wet-etching parameters yielded a facet with an average sidewall angle of 0.7° from vertical and less than 2-nm RMS roughness, corresponding to a facet reflectivity greater than 95% of an ideal AlGaN/air interface. No preferential etching was observed for $Al_xGa_{1-x}N$ alloys with compositions in the range x=0-0.5, indicating that this is an effective method to prepare high-reflectivity facets for deep-UV laser diodes.

Finally, packaged laser diodes were tested and revealed robustness to an impressively high 30 kA/cm^2. These high current densities yielded very bright electroluminescence (spontaneous emission), however no stimulated emission was observed. Future studies, examining both

defect-related current leakage paths as well as doping-dependent cavity loss, are expected to be critical final steps to achieving stimulated emission at 340 nm and shorter deep UV wavelengths.

6. REFERENCES

1. A. J. Fischer, A. A. Allerman, M. H. Crawford, K. H. A Bogart, S. R. Lee, R. J. Kaplar, W. W. Chow, S. R. Kurtz, K. W. Fullmer, and J. J. Figiel, Appl. Phys. Lett. 84, 3394 (2004)

2. H. Yoshida, Y. Yamashita, M. Kuwabara, and H. Kan, Appl. Phys. Lett. 93, 241106.

3. K. Iida, H. Watanabe, K. Takeda, T. Nagai, T. Sumii, K. Nagamatsu, T. Kawashima, K. Balakrishnan, M. Iwaya, S. Kamiyama, H. Amano, I. Akasaki, and A. Bandoh, phys. stat. sol. (a) 204, (2007) 2000

4. S. R. Lee, A. M. West, A. A. Allerman, K. E. Waldrip, D. M. Follstaedt, P. P. Provencio, D. D. Koleske and C. R. Abernathy, Appl. Phys. Lett., 86, (2005) 241904.

5. S. F. Chichibu, A. Uedono, T. Onuma, B. A. Haskell, A. Chakraborty, T. Koyama, P. T. Fini, S. Keller, S. P. DenBaars, J. S. Speck, U. K. Mishra, S. Nakamura, S. Yamaguchi, S. Kamiyama, H. Amano, I. Akasaki, J. Han, and T. Sota, Nat. Mater. **5**, 810 (2006).

6. Koida, S. F. Chichibu, T. Sota, M. D. Craven, B. A. Haskell, J. S. Speck, S. P. DenBaars, and S. Nakamura, Appl. Phys. Lett. **84**, 3768 (2004).

7. G. A. Garrett, A.V. Sampath, C. J. Collins, E. D. Readinger, W. L. Sarney, H. Shen, M. Wraback, V. Soukhoveev, A. Usikov, and V. Dmitriev, phys. stat. sol. (c) **3**, 2125 (2006).

8. G. A. Garrett, C. J. Collins, A. V. Sampath, H. Shen, M. Wraback, S. F. LeBoeuf, J. Flynn, and G. Brandes, phys. stat. sol. (c) **2** 2332 (2005).

9. S. F. Chichibu, T. Onuma, K. Hazu, and A. Uedono, Appl. Phys. Lett. **97**, 201904 (2010).

10. A. Chantre, G. Vincent, and D. Bois, Phys. Rev. B **23**, 5335 (1981).

11. G. Lucovsky, Solid State Commun. **3** 299–302 (1965).

12. R. Pässler, J. Appl. Phys. **96**, 715 (2004).

13. N. Nepal, M. L. Nakarmi, J. Y. Lin, and H. X. Jiang, Appl. Phys. Lett. **89**, 092107 (2006).

14. G-C Yi and B. W. Wessels, Appl. Phys. Lett. **68**, 3769 (1996).

15. A. Hierro, D. Kwon, S. A. Ringel, M. Hansen, J. S. Speck, U. K. Mishra, and S. P. DenBaars, Appl. Phys. Lett. **76**, 3064 (2000).

16. J. Li, T. N. Oder, M. L. Nakarmi, J. Y. Lin, and H. X. Jiang, Appl. Phys. Lett., **7**, (2002) 1210-1212.

17. E. F. Schubert, W. Grieshaber, and I. D. Goepfert, Appl. Phys. Lett. **69**, (1996) 3737-3739.

18. K. Kumakura, and N. Kobayashi, Jpn. J. Appl. Phys. **38**, (1999) L1012-1014.

19. I. D. Geophert, E. F. Schubert, A. Osinsky, and P. E. Norris, Electronics Lett. **24**, (1999) 1109-1111.

20. P. Kozodoy, M. Hansen, S. P. DenBaars, U. K. Mishra, Appl. Phys. Lett. **74**, (1999) 3681-3683.

21. S. Nakamura, M. Senoh, S. Nagahama, N. Iwasa, T. Yamada, T. Matsushita, H. Kiyoku, Y. Sugimoto, T. Kozaki, H. Umemoto, M. Sano, and K. Chocho, Jpn. J. Appl. Phys. **35**, (1997) L1568-L1571.

22. G. Kipshidze, V. Kuryatkov, B. Borisov, M. Holtz, S.A. Nikishin, H. Temkin, Appl. Phys. Lett. **80**, (2002) 3682-3684.

23. V. Kuryatkov, A. Chandolu, B. Borisov, G. Kipshidze, K. Zhu, S. A. Nikishin, H. Temkin and M. Holtz, Appl. Phys. Lett., 82, (2003) 1323-1235.

24. S.A. Nikishin, M. Holtz, H. Temkin, Jpn. J. Appl. Phys. **44**, (2005) 7221-7226.

25. S.A. Nikishin, B. Borisov, V. Kuryatkov, M. Holtz, G. A. Garrett, W. L. Sarney, A. V. Sampath, H. Shen, M. Wraback, A. Usikov, V. Dmitriev, J. Mater Sci: Mater Electron **19**, (2008) 764-769.

26. S. R. Lee, A. M. West, A. A. Allerman, K. E. Waldrip, D. M. Follstaedt, P. P. Provencio, D. D. Koleske and C. R. Abernathy, Appl. Phys. Lett., **86**, (2005) 241904.

27. SIMS measurements were made by Evans Analytical Group in Sunnyvale, CA. T. Tanka, A. Watanabe, H. Amano, Y.Kobayashi, I. Akasaki, S. Yamazaki and M. Koike, Appl. Phys. Lett., **65** (1994) 593-594.

28. K Kumakura, T. Makimoto and N. Kobayashi, Jpn. J. Appl. Phys., **39** (2000) 2428-2430.

29. D. A. Stocker, E. F. Schubert, W. Grieshaber, K. S. Boutros, and J. M. Redwing, Appl. Phys. Lett. **73**, 1925 (1998).

30. V. Schwegler, S. S. Schad, M. Scherer, M. Kamp, G. Ulu, M. Emsley, M. S. Unlu, A. Lell, S. Bader, B. Hahn, H. J. Lugauer, F. Kuhn, A. Weimar, V. Harle, J. Cryst. Growth **512-3**, 230 (2001).

31. M. P. Mack, G. D. Via, A. C. Abare, M. Hansen, P. Kozodoy, S. Keller, J. S. Speck, U. K. Mishra, L. A. Coldren, and S. P. DenBaars, Electon. Lett. **34**, 1315 (1998).

32. C. Ambe, T. Takeuchi, H. Katoh, K. Isomura, T. Satoh, R. Mizumoto, S. Yamaguchi, C. Wetzel, H. Amano, I. Akasaki, Y. Kaneko, N. Yamada, Mater. Sci. Eng. B **59**, 382 (1999).

33. F. A. Khan, L. Zhou, A. T. Ping, and I. Adesida, J. Vac. Sci. Technol. *B* **17**, 2750 (1999).

34. C. H. Chen, S. J. Chang, Y. K. Su, G.C. Chi, J. K. Sheu, and I. C. Lin, Jpn. J. Appl. Phys. **40**, 2762 (2001).

35. C. Youtsey and I. Adesida, "Advanced Plasma Processing Techniques," Eds. R .J. Shul and S. J. Pearton, Springer-Verlag., 483-494 (1999).

36. M. Kneissl, D. Hofstetter, D. P. Bour, R. Donaldson, J. Walker, and N. M. Johnson, J. Cryst. Growth **189/190**, 846 (1998).

37. A. T. Ping, I. Adesida, and M. Asif Khan, Appl. Phys. Lett. **67**, 1250 (1995).

38. D. A. Stocker, E. F. Schubert, and J. M. Redwing, Appl. Phys. Lett. **77**, 4253 (2000).

39. T. Bottcher, C. H. Zellweger, S. Figge, R. Kroger, C. H. Petter, H.-J. Buhlmann, M. Ilegems, P. L. Ryder, and D. Hommel, Phys. Stat. Sol. (a) **191**, R3 (2002).

40. M. Itoh, T. Kinoshita, C. Koike, M. Takeuchi, K. Kawasaki, and Y. Aoyagi, Jpn. J. Appl. Phys. **45**, 3988 (2006).

41. M. Itoh, T. Kinoshita, K. Kawasaki, M. Takeuchi, C. Koike, and Y. Aoyagi, Phys. Stat. Sol. (c) **3**, 1624 (2006).

42. D. Zhuang, and J. H. Edgar, Mater. Sci. Eng. R **48**, 1 (2005).

43. D. Marcuse, J. Lightwave Technol. **7**, 336 (1989).

44. K. Iga, K. Wakao, and T. Kunikane, Appl. Optics **20**, 2367 (1981).

45. G. M. Laws, E. C. Larkins, I. Harrison, C. Molloy, and D. Somerford, J. Appl. Phys. **89**, 1108 (2001).

DISTRIBUTION

1	MS1086	Mary Crawford	01123 (electronic copy)
1	MS1086	Andrew Allerman	01126 (electronic copy)
1	MS1086	Andrew Armstrong	01123 (electronic copy)
1	MS1086	Tanya Henry	01123 (electronic copy)
1	MS1086	Stephen Lee	01123 (electronic copy)
1	MS1086	Daniel Barton	01123 (electronic copy)
1	MS1086	Robert Biefeld	01123 (electronic copy)
1	MS1086	Karen Cross	01126 (electronic copy)
1	MS1086	Michael Smith	01123 (electronic copy)
1	MS1086	Karl Westlake	01123 (electronic copy)
1	MS1086	Leonard Alessi	01126 (electronic copy)
1	MS1086	Mary Miller	01726 (electronic copy)
1	MS0899	RIM-Reports Management	09532
1	MS0359	D. Chavez, LDRD Office	01911


Sandia National Laboratories